Accepted manuscript

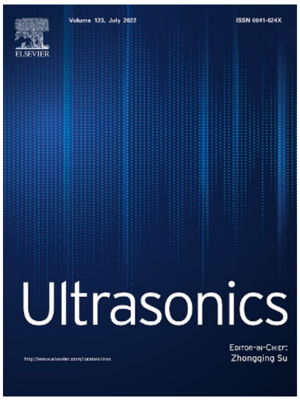

The effect of external load on ultrasonic wave attenuation in steel bars under bending stresses

Adam Sciegaj, Erwin Wojtczak, Magdalena Rucka

In: *Ultrasonics* 124, 106748

DOI: https://doi.org/10.1016/j.ultras.2022.106748

Please cite this article as:

> A. Sciegaj, E. Wojtczak, M. Rucka, The effect of external load on ultrasonic wave attenuation in steel bars under bending stresses, *Ultrasonics* 124 (2022) 106748 , doi: https://doi.org/10.1016/j.ultras.2022.106748

The effect of external load on ultrasonic wave attenuation in steel bars under bending stresses

Adam Sciegaj[1*], Erwin Wojtczak[1], Magdalena Rucka[1]

[1] Department of Mechanics of Materials and Structures, Faculty of Civil and Environmental Engineering, Gdańsk University of Technology, Narutowicza 11/12, 80-233, Gdańsk, Poland,
emails: adam.sciegaj@pg.edu.pl, erwin.wojtczak@pg.edu.pl, magdalena.rucka@pg.edu.pl
* corresponding author

Abstract

The stress state in deformed solids has a significant impact on the attenuation of an ultrasonic wave propagating through the medium. Measuring a signal with certain attenuation characteristics can therefore provide useful diagnostic information about the stress state in the structure. In this work, basic principles behind a novel attenuation-based diagnostic framework are introduced. An experimental study on steel bars under three-point bending was carried out, and finite element analyses were used to numerically model the experiments. Obtained test results showed a strong correlation between the external load and the ultrasonic signal energy, which decreases with increasing load. A similar but positive correlation appeared between the level of attenuation of longitudinal ultrasonic wave signals and the external load, which allowed for efficient estimation of the mid-span bending moment. Upon proper calibration of testing equipment, the change in ultrasonic signal energy can therefore be used as an indicator of the external load level. As a result, this effect has potential applications in non-destructive structural health monitoring frameworks.

Keywords

guided wave propagation; attenuation; bending; stress; steel bars; structural health monitoring; finite element modelling

1. Introduction

Early detection and continuous monitoring of damages in structural components and engineering structures have become one of the most relevant problems that both researchers and practitioners must face nowadays. Over the last few decades, structural health monitoring (SHM) techniques have matured and gained recognition in engineering practice. Although SHM encompasses many different research areas, the underlying concept is to register the structural response under a diagnostic input and analyse the data to extract features that can be attributed to specific defects or flaws in the material [1]. Recently, techniques based on ultrasonic testing have gained popularity.

The ultrasonic method is a non-destructive testing (NDT) technique that can be used to detect damage. This technique has already been successfully used for diagnostics of different structures, e.g., for damage detection in concrete elements [2–5], metallic members [6,7], masonry structures [8,9], composites [10–13] or adhesive joints [14–17]. An ultrasonic transducer or piezoelectric actuator excites an elastic wave, which propagates through the material and is later picked up by sensors located at various positions of the surface of the tested object. Propagation characteristics of ultrasound waves in solids depend on many factors, with the density and elastic properties being the most considered. Additionally, applied or residual stresses present in the material result in the deformation of the medium, which has an impact on the propagating wave. The effect of stress on the velocity of the wave propagating through a solid is referred to as the acoustoelastic effect and has already been extensively studied in [18–20]. To properly describe this effect, third-order elastic constants stemming from Murnaghan's theory of finite deformation [21,22] are needed. Notable examples from the literature considering the study of acoustoelastic effect comprise different materials and loading cases. As such, studies on metal specimens in tension [23–27], compression [28–30] and bending [31–33] are noteworthy. However, the direct use of the acoustoelastic effect is problematic since the relative change of phase velocity is rather small even for isotropic and homogeneous materials.

Rather than basing the testing method on the velocity shift, as described above, the attenuation of the wave can be utilised. This phenomenon denotes the gradual loss of wave intensity travelling through the medium. It is important to keep in mind, that in a solid medium both longitudinal and shear elastic waves can be excited. Similarly, both longitudinal and shear waves are subject to attenuation. This effect has already found wide use in ultrasonic imaging, as different materials exhibit a different amount of attenuation. The attenuation of the elastic wave was shown to be strongly dependent on the microstructure of the material. In the case of polycrystalline materials, this effect has been attributed to elastic wave scattering from grain boundaries [34,35]. At the same time, this phenomenon observed in fibre-reinforced polymers (FRPs) is thought to be the resultant of the viscoelastic nature of fibres and matrix, as well as damping due to interphase and damage [36]. Attenuation of ultrasonic waves has been extensively studied in the literature, e.g., for rocks [37,38], composites [36,39–41], polycrystals [42,43], and cracked concrete [44].

However, the effect of stress/strain present in the material on the attenuation of the bulk ultrasonic wave has not been studied to the same extent. As this effect is more pronounced than the relative phase velocity changes due to the acoustoelastic effect, it provides an attractive potential diagnostic method of estimating the stress state in deformed structural components. Structural health monitoring and non-destructive evaluation systems utilising the change in ultrasonic wave attenuation to infer the stress or external load levels are, to the best of the authors' knowledge, novel and deserve further investigation. Even though noteworthy studies can be found in [45–47], this phenomenon has not been examined under elastoplastic response.

The aim of this research is to take the first step towards the use of ultrasonic wave attenuation in structural health monitoring systems. To develop a diagnostic scheme, the relationship between wave attenuation and stress/external load levels must be first studied and understood. In this study, the relation between the external load level and attenuation of longitudinal ultrasonic guided waves propagating in steel bars was investigated by means of experimental analysis. The bars were loaded in three-point bending such that a clear plastic behaviour was observed. Simultaneously, ultrasonic guided wave signals were emitted at one end of the bars and received at the other. A clear correlation between the external load level, wave attenuation, and ultrasonic signal energy was observed. To further validate the experimental results, numerical simulation was used. With the help of the finite element method (FEM) and a novel staggered quasi-static/dynamic analysis, it was possible to numerically reflect the studied relationship.

The remainder of the paper is structured as follows: some theoretical background concerning wave attenuation and wave energy is given in Section 2. Section 3 contains the description of the research object together with experimental and numerical analyses. Moving on, the results of the experimental measurements and numerical simulations are presented and discussed in Section 4. In the same section, wave attenuation is linked to external load level establishing a diagnostic framework. The paper completes in Section 5 with some concluding remarks and an outlook for future work.

2. Theoretical background

2.1. Ultrasonic wave attenuation

The term *attenuation* used throughout this paper should be associated with all phenomena that cause amplitude decay (energy dissipation) of the wave. Often, damping is used synonymously, but it pertains only to energy dissipation due to a force proportional to velocity. As such, damping should be considered only one possible type of attenuation. Nevertheless, a specific attenuation can be accomplished by allowing for a specific amount of damping [41]. In that case, the usual strategy is to compute the damping ratio ζ, which describes how the vibration amplitude of a specific point decays with time. This approach is particularly useful in ultrasonic wave propagation, as wave packets hit sensors at specific locations multiple times before their energy is dissipated.

To start with, let us assume an ultrasonic wave signal $S(t)$, schematically presented in Figure 1, which illustrates in principle the kind of signal received by a sensor. This signal can be decomposed into an undamped normalised signal $S_n(t)$ with the angular frequency ω, consisting of wave packets, and an exponentially decaying component with an initial amplitude A_0, as

$$S(t) = S_n(t) A_0 e^{-\zeta\omega t}. \tag{1}$$

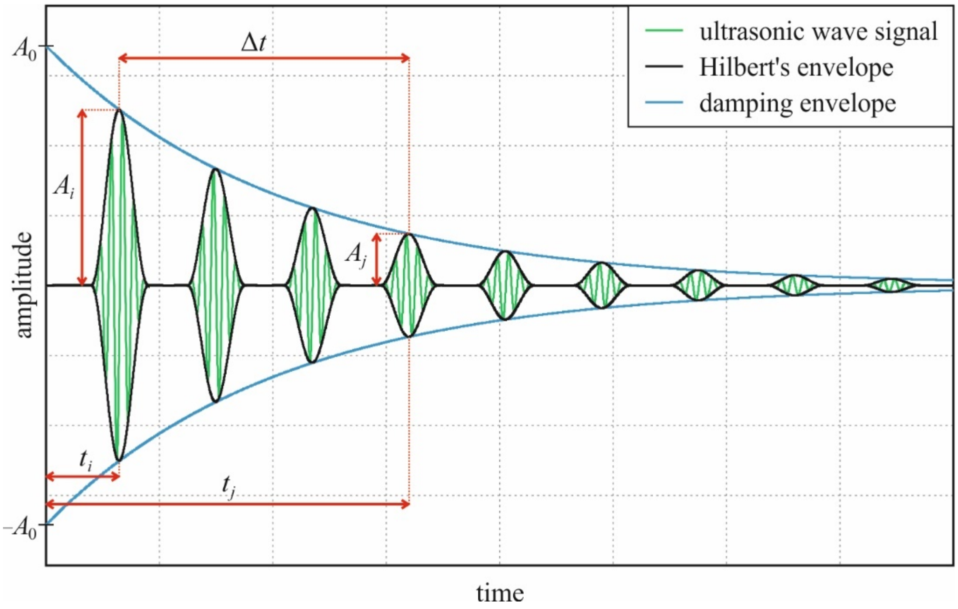

Figure 1: Example of exponentially damped ultrasonic wave signal (green lines) with its Hilbert's envelope (black lines) and exponential damping envelope (blue lines).

Next, let us consider a particular wave amplitude A_i arriving at time t_i, and a smaller amplitude A_j with arrival time t_j. In addition, it is assumed that the time difference $\Delta t = t_j - t_i$ is a multiple of the wave period T, i.e., $\Delta t = nT$. Relating the amplitudes to each other, the value of logarithmic decrement, δ, can be calculated as

$$\delta = \frac{1}{n} \ln\left(\frac{A_i}{A_j}\right). \tag{2}$$

Subsequently, the relation between the damping ratio ζ and the logarithmic decrement can be expressed as

$$\delta = \frac{2\pi\zeta}{\sqrt{1-\zeta^2}}. \tag{3}$$

For a system where ζ is much smaller than one (far from the critical damping case), which is common for most structural elements, the above can be simplified to

$$\delta \approx 2\pi\zeta\ . \tag{4}$$

2.2. Rayleigh damping

A common assumption for the case of vibrations with damping is that the viscous damping force is proportional to the velocity, where the proportionality constant is denoted *c*. In the dynamic analysis, as well as in most finite element (FE) codes, Rayleigh damping is implemented, i.e., the damping coefficient *c* comprises a linear combination of mass *m* and stiffness *k* of the structure

$$c = \alpha m + \beta k, \tag{5}$$

where α and β are the mass and stiffness proportionality coefficients, respectively. These constants can be related to the damping ratio ζ as

$$\zeta = \frac{1}{2}\left(\frac{\alpha}{\omega} + \beta\omega\right). \tag{6}$$

In numerical modelling, either one or both constants can be considered. As a specific case, by eliminating β, the mass proportional factor can be calculated as

$$\alpha = 2\omega\zeta\ . \tag{7}$$

Assuming that the vibration frequency is much higher than the natural frequency of the structure (which is the case for a given ultrasonic signal), the above equation can be applied to determine the mass proportionality coefficient α based on the damping ratio ζ, which can be easily derived from the received wave signals.

2.3. Ultrasonic signal energy

An important characteristic of a signal is its energy. For a continuous time-domain signal $S(t)$ spanning times 0 and *b*, the energy can be computed as

$$E = \int_0^b |S(t)|^2 \, \mathrm{d}t\ . \tag{8}$$

As an example, let us consider a synthetic wave signal $S_c(t)$ expressed mathematically as a cosine function with a particular angular frequency ω damped exponentially with coefficient α, i.e.,

$$S_c(t) = A\cos(\omega t)e^{-\frac{\alpha t}{2}}\ . \tag{9}$$

The energy of such signal calculated between time 0 and *b* can be determined analytically as

$$E = \frac{A^2 e^{-\alpha b}}{2\alpha(\alpha^2 + 4\omega^2)} \cdot (4\omega^2 (e^{\alpha b} - 1) + 2\alpha\omega \sin(2b\omega) - \alpha^2 (1 + \cos(2b\omega) - 2e^{\alpha b})) . \tag{10}$$

From the above, it can be shown that in the limit, i.e., when $e^{-\alpha b}$ is very small, and when the angular frequency ω is much larger than the coefficient α (which is the case for ultrasonic waves), the energy becomes proportional to the square of the amplitude and inversely proportional to α, i.e.,

$$E \propto \frac{A^2}{\alpha} . \tag{11}$$

The classic ultrasonic wave signals received after the excitation in the form of a wave packet are characterised by the periodically repeating waveforms, thus they could not be completely described by a single cosine function. It is, however, important to note that the signal characteristics, like attenuation and amplitude, influence the signals in the same way.

3. Materials and methods

3.1. Description of specimens

The experimental analysis was performed on four steel bars (denoted 1–4) with a cross-section of 5.96 × 5.96 mm^2 and a length of 200 mm. The material density and dynamic Young's modulus were determined experimentally as 7785.16 kg/m^3 and 182.9 GPa, respectively. The latter value was computed according to the procedure developed in [17], with the experimental guided wave dispersion relations first determined. A set of theoretical curves was then calculated for different values of Young's moduli (with other parameters assumed constant) using the GUIGUW software [48], based on semi-analytical finite element formulation (SAFE). The appropriate value of the dynamic Young's modulus was determined as the one for which the theoretical curves provided the best fit to the experimental results.

In addition, three bars (denoted A–C) were examined to characterise the plastic response of the material. Static tensile tests were performed using a Zwick/Roell Z100 testing machine equipped with a contacting extensometer makroXtens II WN (Zwick) until failure of the material. The displacement-controlled testing procedure was applied with a speed of 1 mm/min, and the obtained stress-strain curves can be seen in Figure 2.

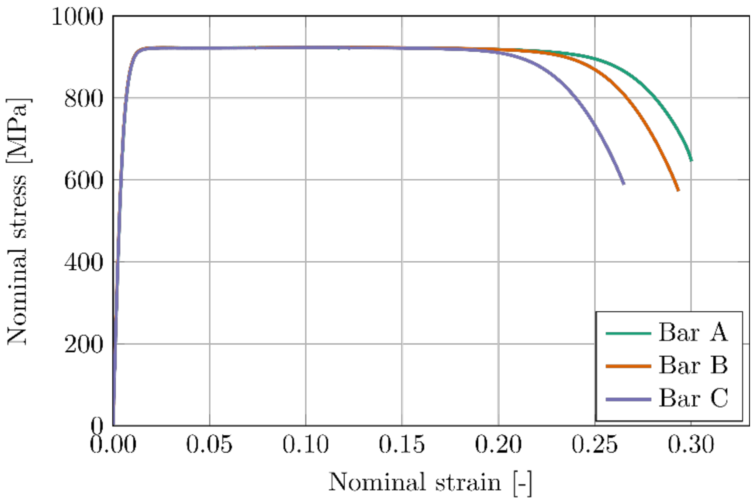

Figure 2: Nominal strain-stress relations for bars A–C obtained from static tensile tests.

To characterise the plastic behaviour of the material, a definition of yield stress is needed. In this case, the stress at which 0.2% plastic strain is reached was considered to be the yield stress and determined to be equal to 812 MPa. Furthermore, it is necessary to provide the relation between the stress and the plastic strain, valid after the yield stress has been reached and prior to necking. For the further numerical simulations in the FE code ABAQUS, the nominal values must be recomputed to true values, given for reference in Figure 3. Respectively, the true stress and strain can be computed from the nominal values as

$$\sigma_{true} = \sigma_{nom}(1+\varepsilon_{nom}), \tag{12}$$

$$\varepsilon_{true} = \ln(1+\varepsilon_{nom}). \tag{13}$$

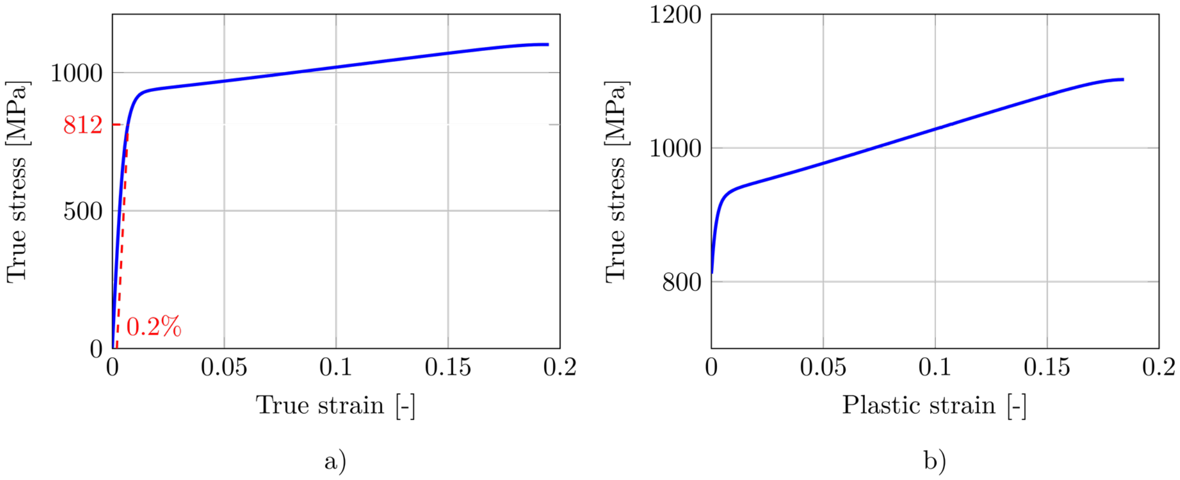

a)

b)

Figure 3: Average true strain-stress relations for the material prior to necking in elastoplastic (a) and inelastic (b) range.

3.2. Experimental setup

The three-point bending tests were performed using a Zwick/Roell Z10 universal testing machine (UTM), with the distance between supports set to 12 cm. A preload of 10 N was applied, after which bending of the bars was carried out with a constant mid-span displacement increment of 2 mm/min. The tests were stopped after 400 s (corresponding to the mid-span displacement of 13.3 mm) and then the samples were unloaded at the same displacement rate.

During quasi-static tests, the bending process was characterized using integrated digital image correlation (DIC) and ultrasonic testing (UT). The experimental setup and instrumentation are shown in Figure 4a. Photographs of the front surface of the bars, covered with a speckle pattern, were taken every 2 s by ARAMIS MC 2D 12M system to measure the displacements. Ultrasonic guided waves were induced and measured in the longitudinal direction with an interval of 2 s. Two multilayer piezoelectric transducers NAC2025 of dimensions 5 mm × 5 mm × 2 mm were used to both excite and register the ultrasonic signals. The transducers were attached to both ends of the bar using petro wax, as shown in Figure 4b. The excitation was a five-cycle wave packet obtained from a 150 kHz frequency sine wave multiplied with a Hann window. The input signals were generated by an arbitrary waveform generator AFG3022C and then amplified by a high voltage amplifier AB A400DI. At the sensor, the signals were received with a sampling rate of 10 MHz by a digital oscilloscope PicoScope 4824. The complete set of experimental data gathered in the course of the three-point bending tests is available at [49].

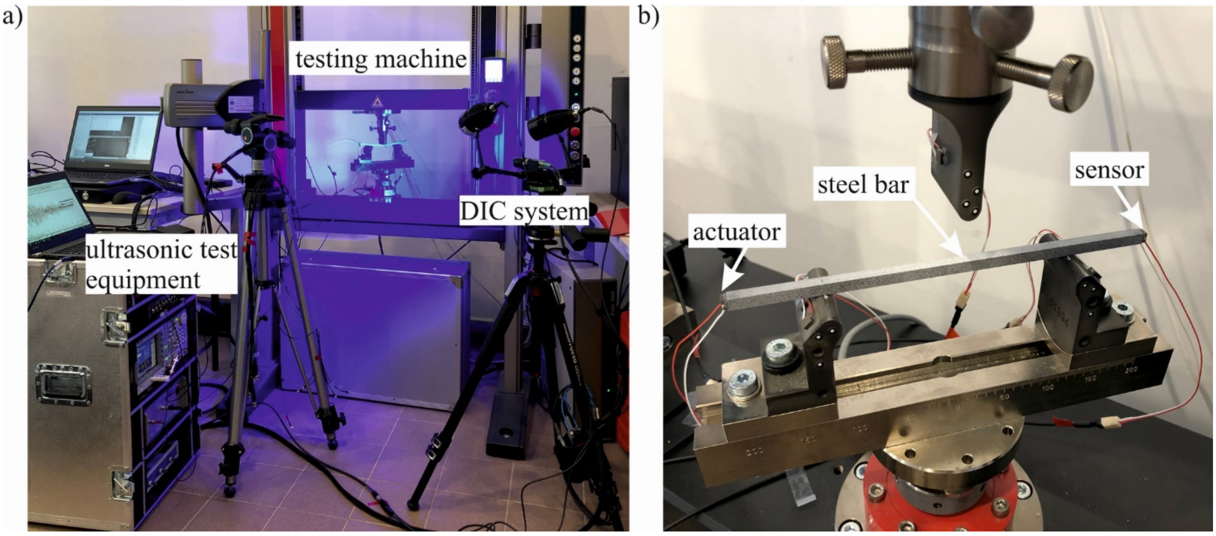

Figure 4: Experimental setup: a) instrumentation for bending test, digital image correlation and ultrasonic testing, b) steel bar with attached piezoelectric transducers.

3.3. Numerical simulations

To investigate the feasibility of numerical modelling of the effect of interest, the experiment described in Section 2.2 was simulated in the finite element software ABAQUS. As the experiment involved three-point bending with simultaneous ultrasound testing, it was simulated by means of staggered quasi-static and dynamic analyses. At the first stage, a quasi-static analysis of the three-point bending tests was performed in ABAQUS/Standard. Subsequently, the model along with its state was imported to ABAQUS/Explicit for wave propagation analysis. The import procedure was repeated multiple times to simulate wave propagation at different stages of the three-point bending test.

3.3.1. Quasi-static analysis

The three-point bending flexural test was modelled in three dimensions. The bar was modelled as a cuboid with a cross-section of 5.96 × 5.96 mm^2 and a length of 200 mm, reflecting the physical specimens. Linear 3D solid cube elements with an approximate size of 0.5 mm were used. As a result, the element size was much less than the length of the 150 kHz ultrasonic wave in steel, ensuring more than 60 nodes per wavelength. For the material, an elastic behaviour up until the yield stress of 812 MPa was considered. The density and Young's modulus were adopted after the experiments as described in Section 2.1, while the Poisson's ratio was assumed as $v = 0.3$. On top of that, plasticity was characterised in terms of true stress and plastic strain according to Figure 3.

To reflect the experimental behaviour in the best way, not only the bar but also the supports and the piston were modelled. These parts were modelled as non-deformable rigid bodies, see Figure 5. Contact interaction between the supports and the lower surface of the bar, as well as between the piston and the upper surface of the bar was then incorporated into the model. To simulate the boundary conditions, both supports were fixed in space. The analysis was run in displacement control, with the vertical position of the rigid piston constituting the controlling parameter of the three-point bending test. At first, the rigid piston was lowered slightly so that contact between all bodies was established. To simulate the first 400 s of the experiment with a loading rate of 2 mm/min, the position of the piston was lowered to a final value of 13.33 mm in 200 steps. To reproduce unloading, the piston was then elevated at the same rate until contact between the bar and the piston was lost, at which point the analysis was terminated. As the ultrasonic waves were emitted every 2 s, each quasi-static load step corresponded to an instant at which the bar was tested with ultrasound.

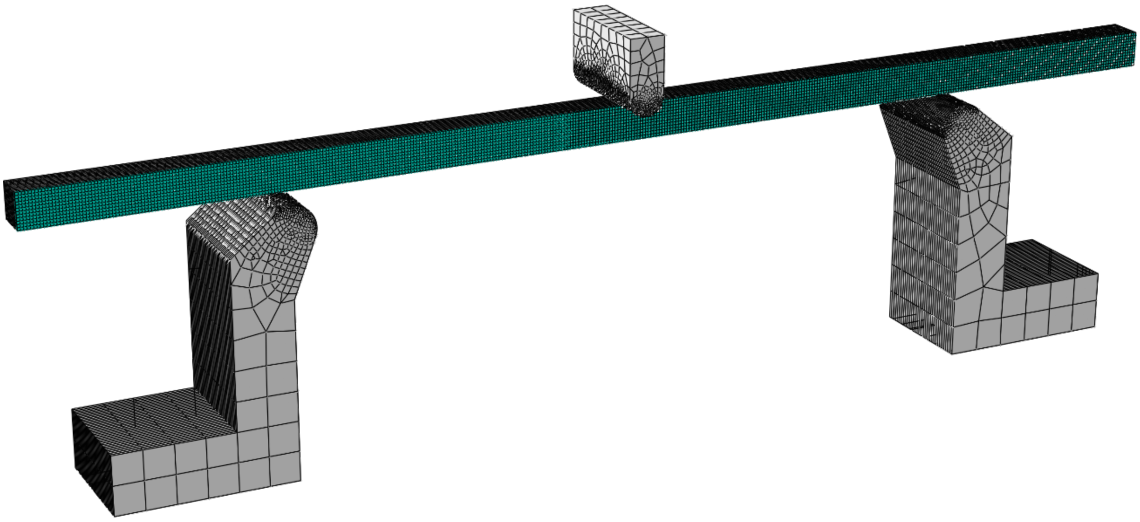

Figure 5: FEM model of the analysed bar under three-point bending with supports and piston marked.

3.3.2. Dynamic analysis

At selected time instances, the state of the numerical model in the quasi-static analysis was saved and subsequently imported into ABAQUS/Explicit for wave propagation analysis. The ultrasonic guided wave propagation was modelled by adequately loading the bar. At one end of the bar, a resultant force of 1 N was applied as surface pressure. Applying the load as pressure instead of a force ensured that the load was applied always in the direction normal to the surface, which changed as loading and unloading progressed. The time-varying amplitude of the pressure was calculated as a five-cycle 150 kHz wave packet windowed with Hann function. Each explicit analysis simulated the first 1.5 ms of ultrasonic wave propagation with 10^{-8} s long time steps. As the output signals received by piezoelectric sensors in experiments can be directly interpreted as acceleration output [50], the accelerations observed at the other end of the bar were considered to simulate the experimental signals. The attenuation was introduced by specifying a suitable Rayleigh damping mass proportionality coefficient α. Numerical values of α were determined based on the experimental results, as described in Sections 2.1 and 2.2.

4. Results and Discussion

4.1. Experimental results

As both the actuator and the sensor were placed around a neutral axis and covered almost the entire cross-section, it was not feasible to distinguish between regions with only tensile or compressive stresses. Moreover, the magnitude of stress changes along the bar according to the magnitude of the bending moment. It was therefore not possible to carefully study the effect of stress state in detail. Any impact on the attenuation was, instead, considered as a global (structural) phenomenon. This way, even though ultrasonic waves partly travelled through regions with variable tensile or compressive stresses, it was possible to quantify and reflect the effect of external load on wave attenuation for the case of three-point bending.

4.1.1. Results of quasi-static and wave propagation tests

The results of experimental measurements for all tested bars (1–4), i.e., changes of external load and signal energy in time, are presented in Figure 6. The repeatability of the results is clearly visible for all load-time curves in Figure 6a. In the initial stage, a linear relation between force and time can be observed. The plastic response can be noticed by the curve winding, which ends at 400 s. After that, the unloading of specimens occurs with a linear decrease of load in time. The relative change of signal energy is presented for all tested bars in Figure 6b. At every quasi-static time instance, signal energy was calculated using Eq. 8. In the calculations, time steps of 10^{-7} s corresponding to the sampling rate of 10 MHz were used. In addition, only the first 1.5 ms of the signals were considered. At first look, the negative correlation between external load and signal energy is evident. The energy was decreasing during loading and increasing at unloading.

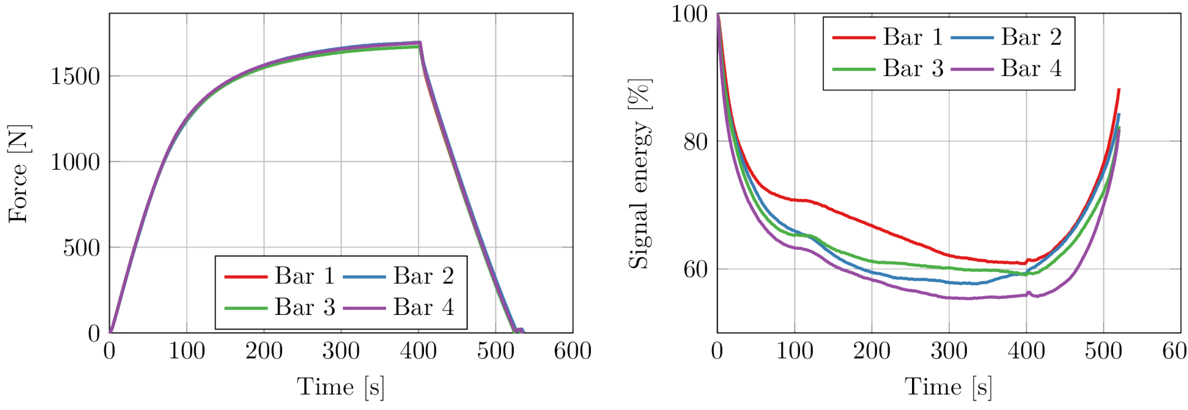

a)

b)

Figure 6: Experimental results for bars 1-4: a) load vs. time curves, b) signal energy vs. time curves.

To quantitatively characterise the agreement between external load and ultrasonic signal energy, correlation coefficients were determined using the Spearman's rank correlation approach, which is suitable for non-linear monotonic relations. The calculations were carried out separately for loading and unloading regions with results presented in Table 1. Negative values indicate an expected negative correlation between both measures (energy decreases with the increasing external load and vice versa). High absolute values (close to one) indicate a strong correlation between variables, which allows for concluding that the relative change in signal energy might be a good indirect measure of the external load level.

Table 1. Spearman's rank correlation coefficients between load and signal energy.

Bar	Loading	Unloading
1	–0.9999	–0.9986
2	–0.9069	–1.0000
3	–0.9995	–0.9989
4	–0.9644	–0.9844

4.1.2. Linking signal energy to attenuation

To better understand the experimentally studied phenomenon, a few other values were determined for the signals, in addition to the already considered signal energy E_1 (computed according to Eq. 8). To begin with, a simple mathematical model of the received signals was necessary. To this end, the signals received at every time instance were modelled as a set of synthetic cosine wave packets, as presented in Section 2.3. Having done that, both the initial amplitude, A, and the attenuation α can be determined. First, the attenuation α was calculated based on the amplitudes of the first two consecutive wave packets in received signals, as described in Sections 2.1 and 2.2. Moving on, the amplitude which provided the best agreement between synthetic and actual signals was determined as an optimal value of A. The energy E_2 of such synthetic signal was then computed according to Eq. 10. The development of the discussed quantities (normalised) in the three-point bending tests is presented for all four bars in Figure 7.

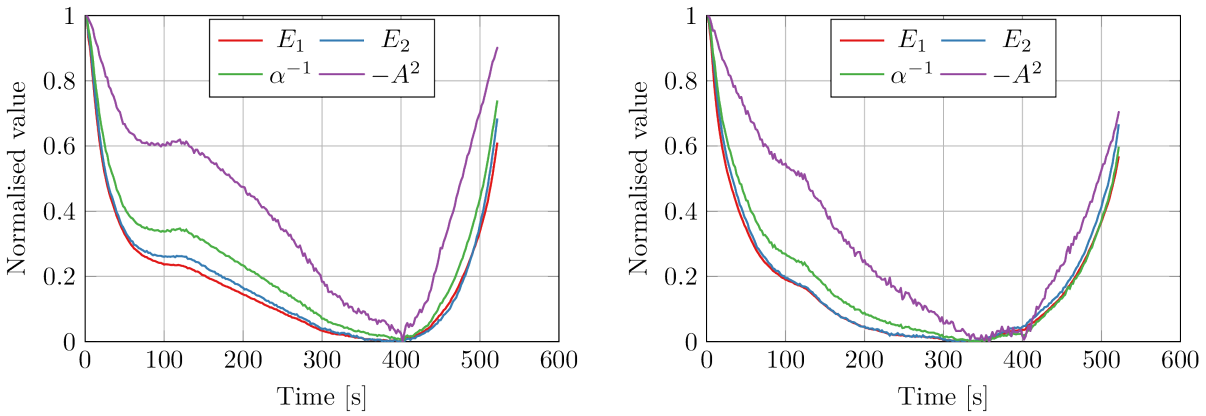

a) Bar 1

b) Bar 2

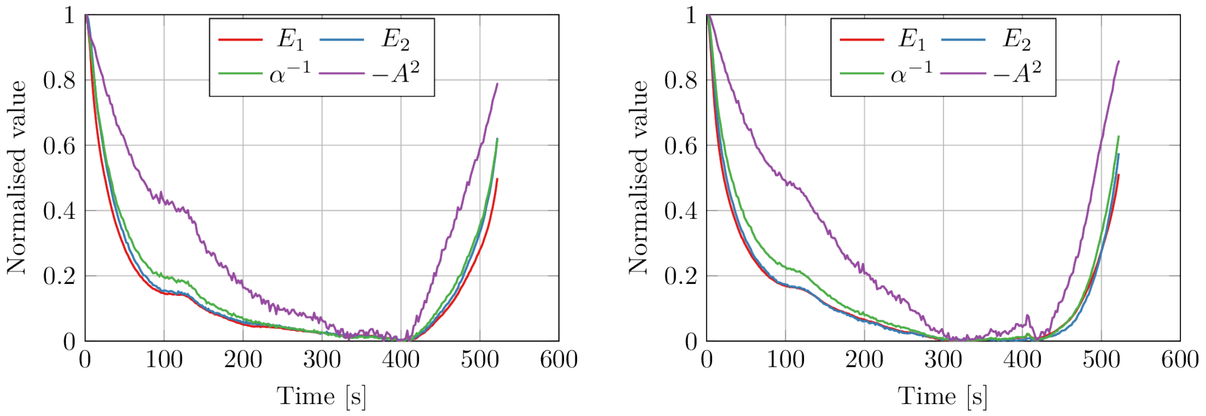

c) Bar 3

d) Bar 4

Figure 7: Development of the relative (normalised) values of signal energies, the inverse of attenuation coefficient, and negative square of the amplitude in three-point bending.

A good correspondence between the actual and synthetic signal energies can be seen in the graphs. Moreover, the inverse attenuation coefficient and the negative square of the determined amplitude also show a strong correlation with the energy, see Table 2 for a quantitative comparison. According to the table, the correlation between signal energy and the inverse of attenuation coefficient is slightly stronger than for the amplitude. This effect can also be seen in Figure 8, where the relations between signal energy and the discussed quantities are plotted for all tested specimens. In the figure, an almost linear relation can be seen for the inverse attenuation coefficient, whereas a clear nonlinear relation between the energy and the square of the amplitude can be observed. It is important to note that the signal values are sensitive, among others, to the input voltage and the quality of the bond between bar and transducer. As such, actual energy values were different for different bars, and although of similar magnitude, could not be directly compared. To amend that, signal energy for the first bar was treated as a reference value, and energies of the remaining signals were scaled appropriately.

Table 2: Spearman's rank correlation coefficients between actual signal energy E_1 and: synthetic signal energy E_2, the inverse of attenuation α^{-1} and negative square of amplitude $-A^2$.

Bar	$r_s(E_1,E_2)$		$r_s(E_1,\alpha^{-1})$		$r_s(E_1,-A^2)$	
	Loading	Unloading	Loading	Unloading	Loading	Unloading
1	0.9991	0.9993	0.9978	0.9992	0.9952	0.9933
2	0.9978	0.9998	0.9699	0.9997	0.9417	0.9988
3	0.9990	0.9992	0.9980	0.9988	0.9942	0.9971
4	0.9795	0.9987	0.9976	0.9974	0.9964	0.9905

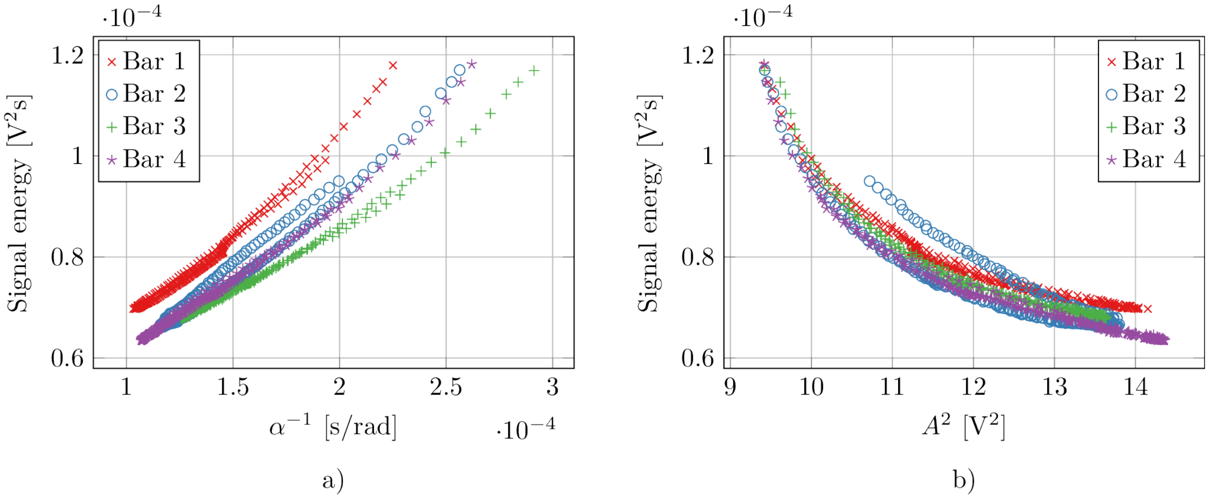

Figure 8: Relation between signal energy and (a) inverse of the attenuation, (b) square of the amplitude.

Last, the correlation between signal energy and the factor $A^2\alpha^{-1}$ is presented in Figure 9. As already shown in Section 2.3, the relation should be mostly proportional, which is the case. Involving the amplitude parameter provides a slightly better correlation, especially at higher signal energy values, but overall, the effect is not that significant and could be omitted for the sake of simplicity.

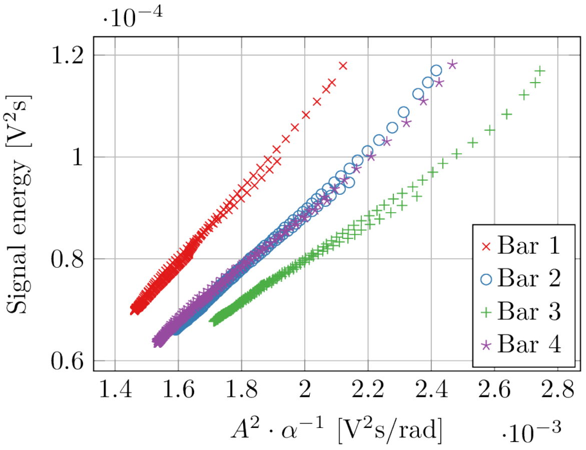

Figure 9: Proportionality of signal energy and $A^2\alpha^{-1}$.

4.2. Numerical results

4.2.1. Quasi-static analysis

To assess the validity of the numerical simulations, relations between the external force and mid-span deflection, presented in Figure 10, should be analysed. In the model, the external force was obtained as the vertical reaction force acting on the rigid piston. The mid-span displacement, readily available in the numerical simulation as the control parameter, was obtained with the help of the DIC system in case of the experiments. The experimental results shown in the graph do not show much variability. At the same time, the numerical result is in good agreement with experiments, with the ultimate load capacity slightly overestimated. To verify the credibility of performed simulation, the effective von Mises stresses are visualized for a specific step of analysis (step 200, at maximum force), see Figure 11. The obtained stress distribution is as expected, extreme values are present at the upper and lower surface of the bar with almost stress-free conditions in the centre (in neutral axis).

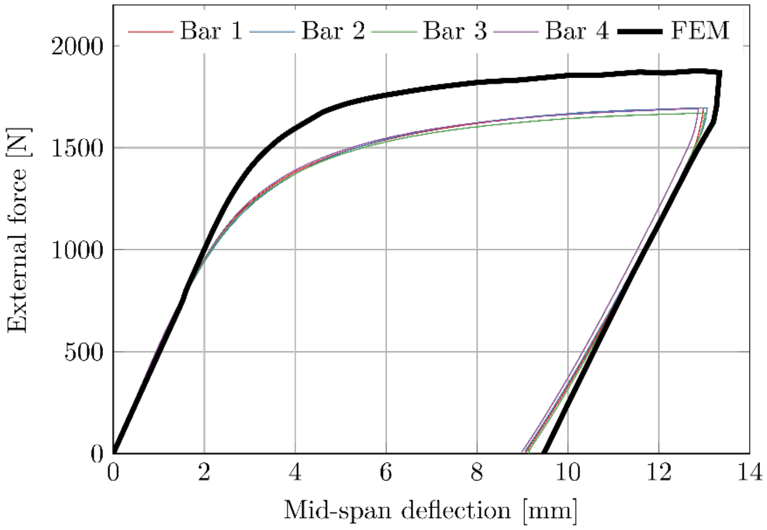

Figure 10: External force versus mid-span deflection – experimental and numerical results.

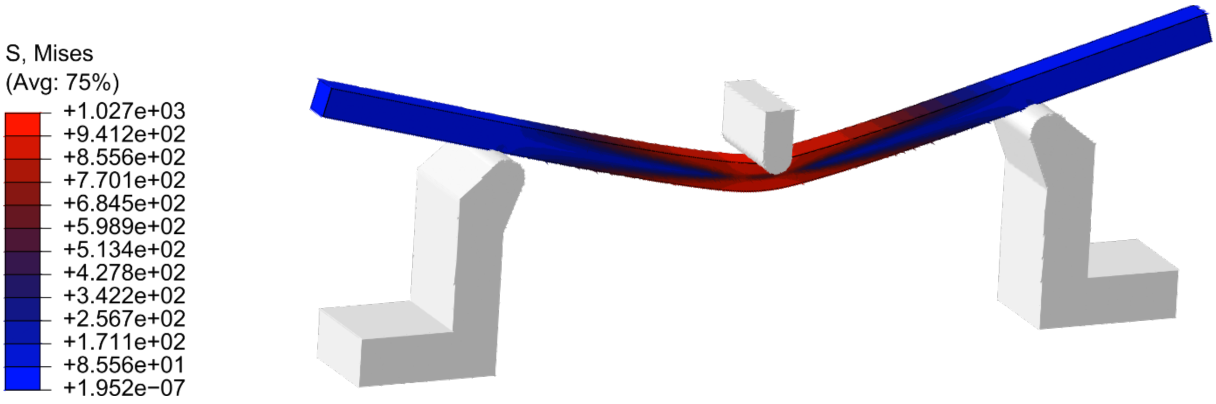

Figure 11: Contour plot of effective von Mises stress at load step 200 (experiment time 400 s).

4.2.2. *Wave propagation analysis*

Wave propagation analyses, as described in Section 3.3.2, were carried out at every tenth quasi-static load step. As already alluded to, surface pressure was applied at one end of the bar, and accelerations (in global directions) obtained at the other end were considered to represent the voltage signal received in the experiments. The accelerations were extracted for a single node located in the centre of the cross-section. Since surface normal was different at every quasi-static time mark, the accelerations were transformed from the global coordinate system to a local one, which followed the deformed shape of the bar. As an example, the magnitude of the acceleration is presented in Figure 12, where the ultrasonic wave is propagating from the left side of the bar.

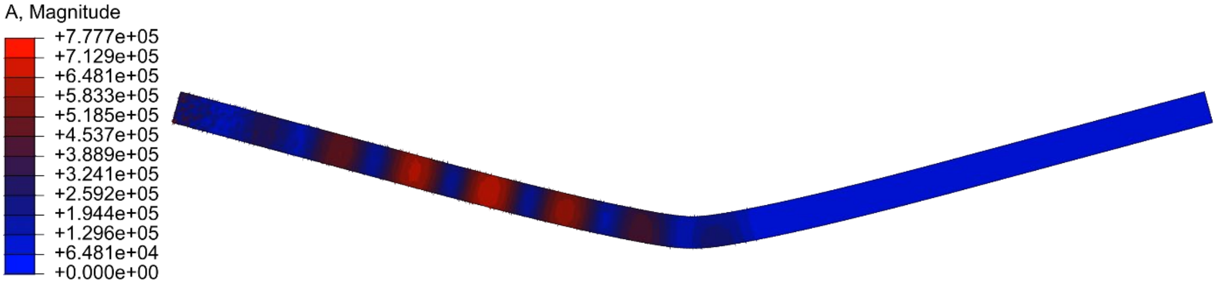

Figure 12: Magnitude of acceleration at time $3 \cdot 10^{-5}$ s in wave propagation analysis. State imported from quasi-static load step 200 (experiment time 400 s).

To compare the experimental and numerical results in a meaningful way, the signals were normalised such that the maximum absolute value in the first wave packet was 1. Ultrasonic signals obtained from the numerical analyses are compared with the experiment on the first bar at few different quasi-static times in Figure 13.

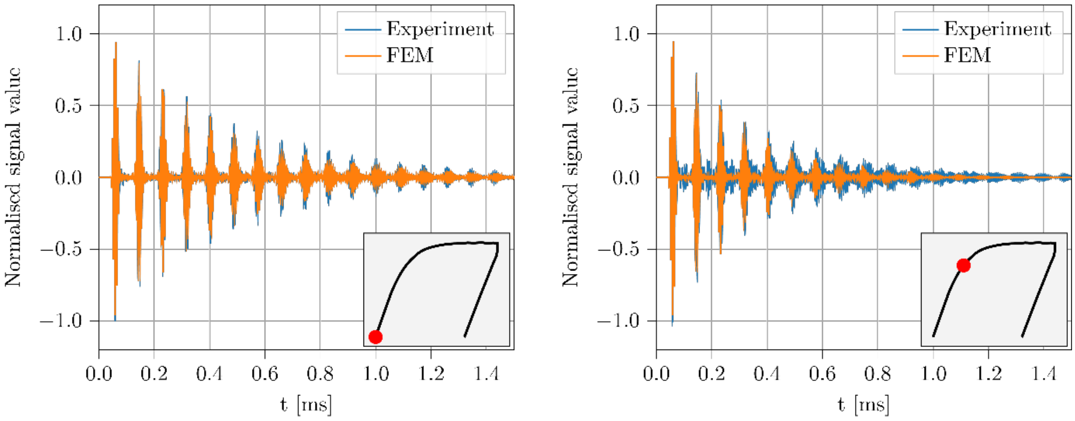

a) Load step 0 (experiment time 0 s) b) Load step 50 (experiment time 100 s)

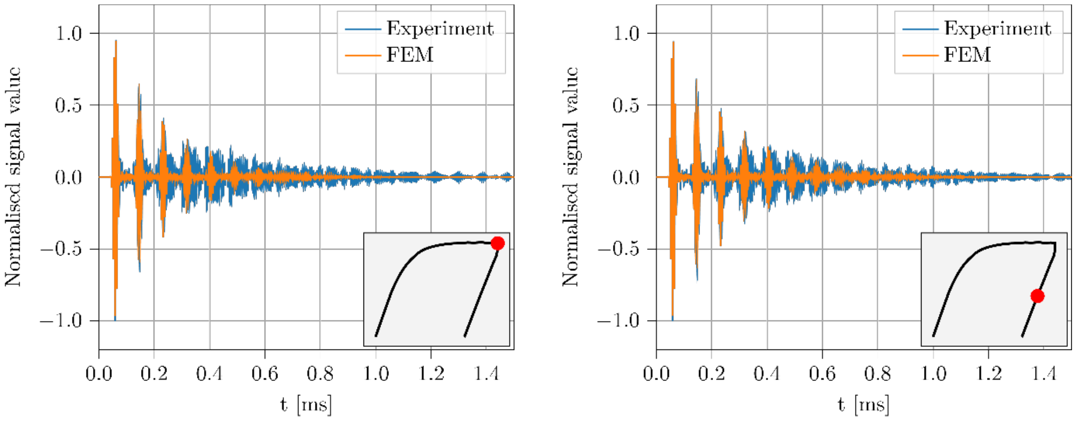

c) Load step 200 (experiment time 400 s) d) Load step 230 (experiment time 460 s)

Figure 13: Normalised ultrasonic signals from numerical analyses and experiment on the first bar. Temporal locations of the experiment/analysis are schematically represented on force-deflection curves.

Few things are noteworthy while looking at the signals. First, there is a good agreement between numerical and experimental results, especially for the first few wave packets, which are thought to carry most of the information about the stress state in the structure. The amplitudes of the first few wave packets agree well. Second, the increase in attenuation of the wave with loading (and a corresponding decrease at unloading) is clearly visible. In the case of numerical analysis, wave dispersion is visible, especially at earlier load steps. At later load steps, the numerical signals decay much quicker than experimental ones. These, in turn, exhibit a high amount of noise in between the wave packets. In fact, it is rather difficult, in the case of experimental results, to identify individual wave packets after the first 3 or 4 peaks. This effect is compounded when the structure is in a plastic regime. It is thought that this could be the effect of the strongly deformed shape of the bar, with the wave travelling at a curved path and interacting with both supports and the piston.

As already mentioned in Section 2.3, the relative change of signal energy can be a good indicator of the stress state or the amount of attenuation for the structure. Energies computed for the first 1.5 ms of numerical and experimental signals are presented in Figure 14. The absolute values of signal energies as a function of experiment time are presented on the left (Figure 14a). They show the same trend, with the energy decreasing at loading and increasing at unloading. At the same time, the energies calculated from numerical signals were noticeably lower than their experimental counterpart. This is not surprising as the numerical signal showed a much lower amount of noise in between the peaks. Normalised energies are shown on the right (Figure 14b). The correlation coefficient between the energies was found to be 0.99. Furthermore, it seems that the numerical signals tended to lose energy at a slightly lower rate than in the experiment, which could be explained by various imperfections present during experimental testing.

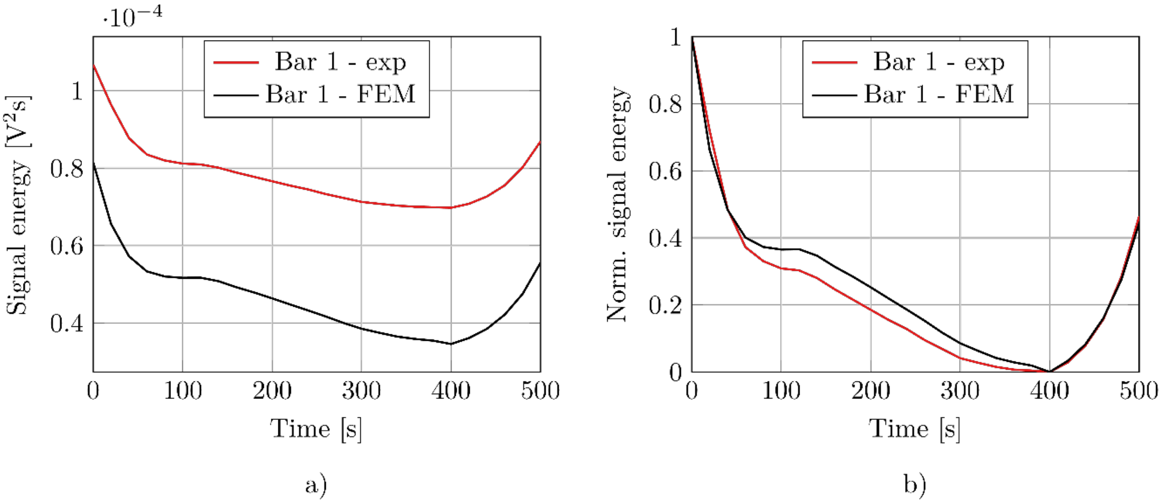

Figure 14: Absolute (a) and normalised (b) energy during the first 1.5 ms for numerical and experimental signals.

4.3. Attenuation-based SHM framework

Having established that the attenuation coefficient *α* (or rather its inverse) makes up for most of the correlation with received signal energy, a natural consequence is to focus on it not only in numerical modelling, but also in in-situ diagnostic testing. While the amplitude of a synthetic cosine wave, *A*, is usually found by an optimisation algorithm offline, α can be efficiently calculated for a signal just by considering the amplitudes of the first wave packets. Nevertheless, the actual numerical value of *α* will be strongly dependent on the experimental conditions, i.e., the quality of the equipment and accuracy of setup. Therefore, a calibration of the testing/monitoring equipment will generally be necessary before the results can be properly interpreted. However, once the equipment is calibrated, the relative changes in attenuation of the signals under external load are believed to be a function of the material, structural geometry, boundary conditions and load case.

Ideally, a single value of α would enable the inference of the stress state in the medium upon proper calibration of the monitoring equipment. In the case of three-point bending, the relation between the average value of α and the average mid-span bending moment is presented in Figure 15:, based on the experimental results.

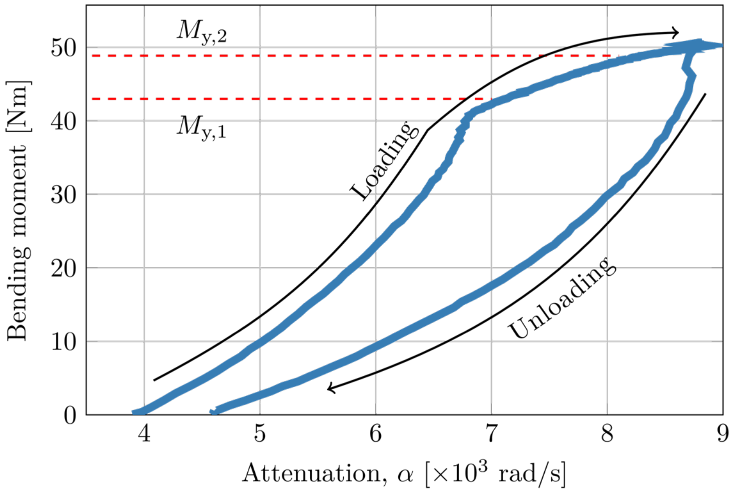

Figure 15: Experimental relation between average mid-span bending moment and average attenuation coefficient for the case of three-point bending.

In the figure, two important levels are marked. Namely, $M_{y,1}$ is the theoretical bending moment when the yield stress (here 812 MPa) is reached at the outermost fibres of the cross-section. Similarly, $M_{y,2}$ stands for the theoretical bending moment when maximum nominal stress (here 923 MPa) is present throughout the cross-section, i.e., plastic capacity is reached and a plastic hinge is formed. The behaviour hints at a possible hysteresis, with plastic strains having an impact on the overall attenuation coefficient.

It is noteworthy that the presented relation is, in general, valid only for the specific three-point bending test (including the used testing equipment) described in this paper. As such, it is probably not possible to generalise it directly to other tests and different bar dimensions. Nevertheless, it shows that upon correct calibration of the diagnostic system (and perhaps using an extensive database covering a wider range of structures), internal forces could be inferred with a simple calculation of the attenuation coefficient α. This general principle could be further used in novel structural health monitoring systems based on ultrasonic signal attenuation.

5. Conclusions

In this paper, the effect of external load on the attenuation of longitudinal ultrasonic guided waves during elastoplastic three-point bending of steel bars was studied, with both experimental and numerical investigations carried out. The attenuation coefficients were calculated from received signals by considering the amplitudes of first wave packets. It was found that the attenuation was strongly correlated with signal energy and the external load, such that a higher external load resulted in lower signal energy. Similarly, a larger attenuation coefficient could be observed for increasing external load. A clear hysteresis effect was observed with respect to signal energy and attenuation coefficient upon unloading the specimens. Furthermore, a series of staggered quasi-static and dynamic finite element analyses showed that a suitable Rayleigh damping could be used to properly simulate this effect numerically. Considering that to calculate attenuation, only the relative levels of the consecutive peaks of the wave packets are needed, the experimental behaviour was reflected in the numerical results well. Similarly, the signal energy of the numerical signals agreed with the measured energy.

This research takes the first step towards a novel use of ultrasonic wave attenuation in structural health monitoring systems. Even though longitudinal wave attenuation may be a rare situation in non-destructive testing and structural health monitoring, the theoretical foundations laid in this work could be used as a basis upon which methods and systems could be built. Such systems would use the empirically observed attenuation-load relation and allow for inference of the external load and stress state in structural components and engineering structures based on the relative changes of signal energy and attenuation. Alternatively, continuous monitoring systems picking up a relative change in signal energy could indicate a potential change in internal forces and, in turn, the risk of damaging parts of the structure. At the present, the load-attenuation relation was analysed empirically and needs to be calibrated before each specific test. However, it may be possible to come up with a physically-based mathematic model which describes this phenomenon. For that, however, it may be necessary to base this model on numerous material and geometrical parameters.

For future work, many details remain to be studied further. First of all, more complex structures should be studied with regard to the described phenomena. To start, structures with different geometry, as well as with different external load and boundary conditions should be investigated. For this reason, it is necessary to extend the analysis to transverse ultrasonic waves, as it is not always possible to place transducers such that a longitudinal wave is guided through the medium. Similarly, a wider frequency range of the waves should be covered so that possible dispersion phenomena can be understood. Furthermore, the hysteresis effect and the influence of inelastic deformation should be given a closer look by considering cyclic loading and residual stresses. Finally, given sufficient experimental testing, this phenomenon should be generalised from a structural effect to relations valid at material point level, i.e., to relate attenuation to stress and strain state. Having done that, the methodology could be used for both modelling wave propagation and diagnostic testing of other materials, e.g., sensing cracks and localised damage zones in concrete structures.

Acknowledgements

The study was financed by the National Science Centre, Poland, with project No. 2019/35/B/ST8/01905. Calculations were carried out at the Centre of Informatics Tricity Academic Supercomputer & Network.

References

[1] M. Mitra, S. Gopalakrishnan, Guided wave based structural health monitoring: A review, Smart Mater. Struct. 25 (2016) 53001. https://doi.org/10.1088/0964-1726/25/5/053001.

[2] M. Rucka, K. Wilde, Experimental Study on Ultrasonic Monitoring of Splitting Failure in Reinforced Concrete, J. Nondestruct. Eval. 32 (2013) 372–383. https://doi.org/10.1007/s10921-013-0191-y.

[3] K. Schabowicz, Ultrasonic tomography - The latest nondestructive technique for testing concrete members - Description, test methodology, application example, Arch. Civ. Mech. Eng. 14 (2014) 295–303. https://doi.org/10.1016/j.acme.2013.10.006.

[4] A. Garbacz, T. Piotrowski, L. Courard, L. Kwaśniewski, On the evaluation of interface quality in concrete repair system by means of impact-echo signal analysis, Constr. Build. Mater. 134 (2017) 311–323. https://doi.org/10.1016/j.conbuildmat.2016.12.064.

[5] L. Pahlavan, F. Zhang, G. Blacquière, Y. Yang, D. Hordijk, Interaction of ultrasonic waves with partially-closed cracks in concrete structures, Constr. Build. Mater. 167 (2018) 899–906. https://doi.org/https://doi.org/10.1016/j.conbuildmat.2018.02.098.

[6] T. Stepinski, Novel instrument for inspecting rock bolt integrity using ultrasonic guided waves, Meas. J. Int. Meas. Confed. 177 (2021) 109271. https://doi.org/10.1016/j.measurement.2021.109271.

[7] T. Yu, W. Guo, C. Miao, J. Zheng, Z. Hua, Study on inserted curved surface coupling phased array ultrasonic inspection of multi-layered steel vessel for high-pressure hydrogen storage, Int. J. Hydrogen Energy. 46 (2021) 18433–18444. https://doi.org/10.1016/j.ijhydene.2021.02.226.

[8] H. Paasche, A. Wendrich, J. Tronicke, C. Trela, Detecting voids in masonry by cooperatively inverting P-wave and georadar traveltimes, J. Geophys. Eng. 5 (2008) 256–267. https://doi.org/10.1088/1742-2132/5/3/002.

[9] M. Zielińska, M. Rucka, Non-Destructive Assessment of Masonry Pillars using

Ultrasonic Tomography, Materials (Basel). 11 (2018) 2543. https://doi.org/10.3390/ma11122543.

[10] P. Aryan, A. Kotousov, C.T. Ng, B.S. Cazzolato, A baseline-free and non-contact method for detection and imaging of structural damage using 3D laser vibrometry, Struct. Control Heal. Monit. 24 (2017) 1–13. https://doi.org/10.1002/stc.1894.

[11] Ł. Pieczonka, Ł. Ambroziński, W.J. Staszewski, D. Barnoncel, P. Pérès, Damage detection in composite panels based on mode-converted Lamb waves sensed using 3D laser scanning vibrometer, Opt. Lasers Eng. 99 (2017) 80–87. https://doi.org/10.1016/j.optlaseng.2016.12.017.

[12] R.K. Munian, D.R. Mahapatra, S. Gopalakrishnan, Lamb wave interaction with composite delamination, Compos. Struct. 206 (2018) 484–498. https://doi.org/10.1016/j.compstruct.2018.08.072.

[13] K. Askaripour, A. Żak, A study on diagnosing both isotropic and orthotropic, intentionally damaged laminates, Nondestruct. Test. Eval. 36 (2021) 237–260. https://doi.org/10.1080/10589759.2020.1740701.

[14] T.Y. Sunarsa, P. Aryan, I. Jeon, B. Park, P. Liu, H. Sohn, A reference-free and non-contact method for detecting and imaging damage in adhesive-bonded structures using air-coupled ultrasonic transducers, Materials (Basel). 10 (2017) 1–16. https://doi.org/10.3390/ma10121402.

[15] M. Rucka, E. Wojtczak, J. Lachowicz, Damage Imaging in Lamb Wave-Based Inspection of Adhesive Joints, Appl. Sci. 8 (2018) 522. https://doi.org/10.3390/app8040522.

[16] F. Nicassio, S. Carrino, G. Scarselli, Elastic waves interference for the analysis of disbonds in single lap joints, Mech. Syst. Signal Process. 128 (2019) 340–351. https://doi.org/10.1016/j.ymssp.2019.04.011.

[17] E. Wojtczak, M. Rucka, Monitoring the curing process of epoxy adhesive using ultrasound and Lamb wave dispersion curves, Mech. Syst. Signal Process. 151 (2021) 107397. https://doi.org/10.1016/j.ymssp.2020.107397.

[18] D.S. Hughes, J.L. Kelly, Second-Order Elastic Deformation of Solids, Phys. Rev. 92 (1953) 1145–1149. https://doi.org/10.1103/PhysRev.92.1145.

[19] F. Bach, V. Askegaard, General stress-velocity expressions in acoustoelasticity, Exp. Mech. 19 (1979) 69–75. https://doi.org/10.1007/BF02324528.

[20] Y.-H. Pao, Theory of Acoustoelasticity and Acoustoplasticity, in: J.D. Achenbach, Y. Rajapakse (Eds.), Solid Mech. Res. Quant. Non-Destructuve Eval., Martinus Nijhoff

Publishers, 1987: pp. 257–273.

[21] F.D. Murnaghan, Finite Deformations of an Elastic Solid, Am. J. Math. 59 (1937) 235–260. https://doi.org/10.2307/2371405.

[22] S. Takahashi, Measurement of third-order elastic constants and stress dependent coefficients for steels, Mech. Adv. Mater. Mod. Process. 4 (2018) 0–6. https://doi.org/10.1186/s40759-018-0035-7.

[23] G.S. Kino, J.B. Hunter, G.C. Johnson, A.R. Selfridge, D.M. Barnett, G. Hermann, C.R. Steele, Acoustoelastic imaging of stress fields, J. Appl. Phys. 50 (1979) 2607–2613. https://doi.org/10.1063/1.326268.

[24] J. Frankel, W. Scholz, Ultrasonic Studies of Stresses and Plastic Deformation in Steel During Tension and Compression, Rev. Prog. Quant. Nondestruct. Eval. (1987) 1577–1584. https://doi.org/10.1007/978-1-4613-1893-4_177.

[25] M.I. Albakri, V.V.N.S. Malladi, P.A. Tarazaga, Low-frequency acoustoelastic-based stress state characterization: Theory and experimental validation, Mech. Syst. Signal Process. 112 (2018) 417–429. https://doi.org/10.1016/j.ymssp.2018.04.011.

[26] S. Kocakaplan, J.L. Tassoulas, Wave propagation in initially-stressed elastic rods, J. Sound Vib. 443 (2019) 293–309. https://doi.org/10.1016/j.jsv.2018.11.045.

[27] Z. Li, Y. Wang, J. Zheng, N. Liu, M. Li, J. Teng, Stress measurement for steel slender waveguides based on the nonlinear relation between guided wave group velocity and stress, Meas. J. Int. Meas. Confed. 179 (2021) 109465. https://doi.org/10.1016/j.measurement.2021.109465.

[28] K.F. Bompan, V.G. Haach, Ultrasonic tests in the evaluation of the stress level in concrete prisms based on the acoustoelasticity, Constr. Build. Mater. 162 (2018) 740–750. https://doi.org/10.1016/j.conbuildmat.2017.11.153.

[29] R. Jasiński, Identification of Stress States in Compressed Masonry Walls Using a Non-Destructive Technique (NDT), Materials (Basel). 13 (2020) 2852. https://doi.org/10.3390/ma13122852.

[30] R. Jasiński, K. Stebel, P. Kielan, Use of the AE Effect to Determine the Stresses State in AAC Masonry Walls under Compression, Materials (Basel). 14 (2021) 3459. https://doi.org/10.3390/ma14133459.

[31] M.J. Fisher, G. Herrmann, Acoustoelastic Measurements of Residual Stress, in: Rev. Prog. Quant. Nondestruct. Eval., 1994: pp. 1283–1291.

[32] M.O. Si-Chaib, S. Menad, H. Djelouah, M. Bocquet, An ultrasound method for the acoustoelastic evaluation of simple bending stresses, NDT E Int. 34 (2001) 521–529.

https://doi.org/10.1016/S0963-8695(01)00012-3.

[33] M.O. Si-Chaib, H. Djelouah, T. Boutkedjirt, Propagation of ultrasonic waves in materials under bending forces, NDT E Int. 38 (2005) 283–289. https://doi.org/10.1016/j.ndteint.2004.09.008.

[34] C.M. Kube, J.A. Turner, Stress-dependent ultrasonic scattering in polycrystalline materials, J. Acoust. Soc. Am. 139 (2016) 811–824. https://doi.org/10.1121/1.4941253.

[35] A. Van Pamel, C.R. Brett, P. Huthwaite, M.J.S. Lowe, Finite element modelling of elastic wave scattering within a polycrystalline material in two and three dimensions, J. Acoust. Soc. Am. 138 (2015) 2326–2336. https://doi.org/10.1121/1.4931445.

[36] M. Gresil, V. Giurgiutiu, Prediction of attenuated guided waves propagation in carbon fiber composites using Rayleigh damping model, J. Intell. Mater. Syst. Struct. 26 (2015) 2151–2169. https://doi.org/10.1177/1045389X14549870.

[37] W. Yuan, J. Jin, Z. Guo, Y. Wu, Theoretical Analysis of Longitudinal Wave Attenuation in a Stressed Rock With Variable Cross-Section, Front. Earth Sci. 7 (2019) 1–9. https://doi.org/10.3389/feart.2019.00270.

[38] Y. Cheng, Z. Song, J. Jin, J. Wang, T. Wang, Experimental study on stress wave attenuation and energy dissipation of sandstone under full deformation condition, Arab. J. Geosci. 12 (2019). https://doi.org/10.1007/s12517-019-4915-x.

[39] S. Guo, M. Rebillat, N. Mechbal, Spatial attenuation prediction of lamb waves in composite materials, 9th ECCOMAS Themat. Conf. Smart Struct. Mater. SMART 2019. (2019) 1236–1247.

[40] H. Mei, V. Giurgiutiu, Guided wave excitation and propagation in damped composite plates, Struct. Heal. Monit. 18 (2019) 690–714. https://doi.org/10.1177/1475921718765955.

[41] C. Ramadas, K. Balasubramaniam, A. Hood, M. Joshi, C. V. Krishnamurthy, Modelling of attenuation of lamb waves using rayleigh damping: Numerical and experimental studies, Compos. Struct. 93 (2011) 2020–2025. https://doi.org/10.1016/j.compstruct.2011.02.021.

[42] G. Sha, Attenuation and Phase Velocity of Elastic Wave in Textured Polycrystals with Ellipsoidal Grains of Arbitrary Crystal Symmetry, Acoustics. 2 (2020) 51–72. https://doi.org/10.3390/acoustics2010005.

[43] A.P. Arguelles, J.A. Turner, Ultrasonic attenuation of polycrystalline materials with a distribution of grain sizes, J. Acoust. Soc. Am. 141 (2017) 4347–4353. https://doi.org/10.1121/1.4984290.

[44] L. Zhou, Y. Zheng, H. Ma, G. Song, Attenuation characteristics of stress wave in cracked concrete beam using smart aggregate transducers enabled time-reversal technique, J. Intell. Mater. Syst. Struct. 32 (2021) 473–485. https://doi.org/10.1177/1045389X20953619.

[45] Y.M. Gupta, Stress dependence of elastic-wave attenuation in LiF, J. Appl. Phys. 46 (1975) 3395–3401. https://doi.org/10.1063/1.322244.

[46] P. Finkel, A.G. Zhou, S. Basu, O. Yeheskel, M.W. Barsoum, Direct observation of nonlinear acoustoelastic hysteresis in kinking nonlinear elastic solids, Appl. Phys. Lett. 94 (2009) 2–5. https://doi.org/10.1063/1.3155201.

[47] C.M. Kube, A.P. Arguelles, Pressure influence on elastic wave attenuation in polycrystalline materials, J. Acoust. Soc. Am. 146 (2019) 4183–4189. https://doi.org/10.1121/1.5135004.

[48] P. Bocchini, M. Asce, A. Marzani, E. Viola, Graphical User Interface for Guided Acoustic Waves, J. Comput. Civ. Eng. 25 (2011) 202–210. https://doi.org/10.1061/(ASCE)CP.1943-5487.0000081.

[49] M. Rucka, E. Wojtczak, A. Ścięgaj, Ultrasonic wave propagation and digital image correlation measurements of steel bars under 3-point bending, (2021). https://doi.org/10.34808/xcg2-m422.

[50] C.N. Sathyanarayana, S. Raja, H.M. Ragavendra, Procedure to Use PZT Sensors in Vibration and Load Measurements, Smart Mater. Res. 2013 (2013) 173605. https://doi.org/10.1155/2013/173605.